
Parallax of a Mira variable R Ursae Majoris studied with astrometric VLBI

Akiharu NAKAGAWA¹, Tomoharu KURAYAMA², Makoto MATSUI¹, Toshihiro OMODAKA¹, Mareki HONMA³, Katsunori M SHIBATA³, Katsuhisa SATO³, and Takaaki JIKE³

¹Graduate School of Science and Engineering, Kagoshima University, 1-21-35 Korimoto, Kagoshima-shi, Kagoshima 890-0065, Japan

²Teikyo University of Science, 2525 Yatsusawa, Uenohara-shi, Yamanashi 409-0193, Japan

³Mizusawa VLBI Observatory, National Astronomical Observatory of Japan, 2-12 Hoshi-ga-oka, Mizusawa-ku, Oshu-shi, Iwate 023-0861, Japan

*E-mail: nakagawa@sci.kagoshima-u.ac.jp

Received (reception date); Accepted (acceptation date)

Abstract

We have measured an annual parallax of the Mira variable R Ursae Majoris (R UMa) with the VLBI exploration for Radio Astronomy (VERA). From the monitoring VLBI observations spanning about two years, we detected H₂O maser spots in the LSR velocities ranges from 37 to 42 km s⁻¹. We derived an annual parallax of 1.97±0.05 mas, and it gives a corresponding distance of 508±13 pc. The VLBI maps revealed 72 maser spots distributed in ~110 au area around an expected stellar position. Circumstellar kinematics of the maser spots were also revealed by subtracting a systemic motion in the Hipparcos catalog from proper motions of each maser spots derived from our VLBI observations. Infrared photometry is also conducted to measure a *K* band apparent magnitude, and we obtained a mean magnitude of $m_K = 1.19 \pm 0.02$ mag. Using the trigonometric distance, the m_K is converted to a *K* band absolute magnitude of $M_K = -7.34 \pm 0.06$ mag. This result gives a much more accurate absolute magnitude of R UMa than previously provided. We solved a zero-point of $M_K - \log P$ relation for the Galactic Mira variables and obtained a relation of $M_K = -3.52 \log P + (1.09 \pm 0.14)$. Other long period variables including red supergiants, whose distances were determined from astrometric VLBI, were also compiled to explore the different sequences of $M_K - \log P$ relation.

Key words: Astrometry: — masers(H₂O) — stars: individual(R UMa) — stars: variables:

1 Introduction

Mira variables and Long Period Variables (LPVs) are low- to intermediate-mass ($1 - 8M_\odot$) asymptotic giant branch (AGB) stars that pulsate with a period range of 100 – 1000 days. They are surrounded by large and extended dust and molecular shells, and in sources with mass-loss rate higher than $\sim 10^{-7} M_\odot \text{yr}^{-1}$, we sometimes find maser emissions of H₂O, SiO, or OH (Gail & Sedlmayr 2014; Habing & Olofsson 2003). Because of their

high mass-loss rate, they are also important source to study chemical composition of the universe. Another characteristic of the sources is concerned to their periodic variation. The relation between *K* band apparent magnitude (m_K) and logarithm of pulsation period ($\log P$) of Mira variables is well known in the Large Magellanic Cloud (LMC) (Feast et al. 1989; Ita et al. 2004). If the LMC distance is given, the relation can be converted to a relation of absolute magnitude (M_K) and $\log P$, then

it can be used as a distance indicator. Since there is a metallicity difference between LMC and our galaxy, it is also important to establish this $M_K - \log P$ relation using sources in our own galaxy. Since the LPVs are very bright in infrared, we can use them to probe a region where interstellar extinction is strong such as the direction of the Galactic Center and Galactic plane. However, a construction of the $M_K - \log P$ relation for the Galactic Mira variables has long been difficult because of large errors in M_K due to distance uncertainty. Making use of a high performance of the VERA array (Kobayashi et al. 2003), which is a Japanese VLBI project dedicated to the Galactic astrometry, we aim to construct the $M_K - \log P$ relation for Galactic LPVs.

R Ursae Majoris (R UMa) is an O-rich Mira variable (Knapp et al. 2000) with a pulsation period of 301.6 days (GCVS)¹. The H₂O masers associated with R UMa also exhibit regular periodic variation with a phase lag of ~ 0.3 with respect to the optical light curve (Shintani et al. 2008). Although the Hipparcos satellite has measured the annual parallax of 2.37 ± 1.06 mas (van Leeuwen 2007), its corresponding distance of 422_{-130}^{+341} pc still has a large error and it brings an uncertainty to the absolute magnitude. In this study, we observe this source with VERA to obtain more accurate distance based on an precise astrometry of H₂O maser positions.

A high resolution VLBI map gives an angular distribution of maser spots around the star. Then, a time series of multiple VLBI observations can add kinematic information to the masers. This helps us to understand a global picture of circumstellar medium on the schemes of time and space. In case the maser distribution is relatively isotropic like a Mira variable ‘T Lep’ in our previous study (Nakagawa et al. 2014), a circumstellar kinematics can be derived from an analysis only using VLBI maps. The detailed procedure is given in section 3.4 in Nakagawa et al. (2014). On the other hand, if the number of the maser spots is small or the distribution is far from isotropic, the same procedure can not offer a reliable kinematic picture of the maser spots. In this study, we propose a new method to obtain a kinematics of the circumstellar masers in R UMa.

We solve the $M_K - \log P$ relation of the Galactic Mira variables based on the latest results from astrometric VLBI observations. Infrared photometry is also used to measure an apparent magnitude in K band.

2 Observation and Data Reduction

2.1 VLBI Observations

We have observed H₂O maser emission at the rest frequency of 22.235080 GHz (6₁₆-5₂₃ transition) associated with R UMa at 24 epochs between 2006 April and 2008 July with a typical separation of 1–2 months using the VLBI Exploration of Radio

Astrometry (VERA). The VERA consists of four antennas of 20 m aperture at Mizusawa, Iriki, Ogasawara, and Ishigaki-jima (Kobayashi et al. 2003). An extra-galactic continuum source J1056+7011 was also observed simultaneously with a dual-beam system equipped with the antennas (Kawaguchi et al. 2000) to maximize on-source integration time of each source. This continuum source is used as a position reference in our phase-referencing analysis. Coordinates of the two sources in J2000 equinox are shown in table 1. The two sources are separated by 1.78° with a position angle of 39° on the sky plane. We summarize the observations in table 2. Observation dates and system noise temperatures (T_{sys}) in each station are presented.

The received source signals from two receivers were recorded using the SONY DIR 2000 system with a recording rate of 1024 Mbps in 2-bit quantization, yielding a data with its total bandwidth of 256 MHz. This total bandwidth of 256 MHz was divided into 16 IF channels of 16 MHz bandwidth. One IF channel was assigned for the maser emission from R UMa, while the other 15 IF channels were assigned for continuum emission from the reference source J1056+7011. Correlation was made with the Mitaka FX correlator (Shibata et al. 1998) using the coordinates in table 1. In the correlation process of R UMa, an 8 MHz data including H₂O maser lines out of the 16 MHz data was selected and divided into 512 spectral channels to obtain a frequency spacing of 15.625 kHz, which corresponds to a velocity spacing of 0.2108 km s^{-1} . For the last observation (Obs. ID 24), a broader frequency spacing of 31.25 kHz corresponding to a velocity spacing of 0.4216 km s^{-1} was adopted. For the data of reference source J1056+7011, each IF channel data were divided into 64 spectral channels. The synthesized beam size was typically $1.2 \text{ mas} \times 0.8 \text{ mas}$ with its major axis position angle of 155° .

Calibration and imaging were performed using the Astronomical Image Processing System (AIPS) software package. We performed an amplitude calibration using T_{sys} . Bright continuum sources 3C273B and 4C39.25 were used in a band-pass calibration of the receiver of R UMa, while a position reference source J1056+7011 was used in the calibration for the other receiver.

We used a task FRING to solve residual phase fluctuations of the reference source J1056+7011, and a task CALIB was also used to solve shorter phase fluctuation. Then, the solutions of phase, rate and amplitude were applied to the data of R UMa. The instrumental phase difference between the two receivers, which was measured during each observation using the correlated data of noise signal injected into the two receivers from artificial noise sources installed on a feedome base of the VERA antenna (Honma et al. 2008), was also applied in the reduction process. Since the *a priori* delay tracking model used in the Mitaka correlator was not accurate enough for precise astrometry, we calibrated them based on more accurate delay track-

¹ General Catalog of Variable Stars
<http://heasarc.gsfc.nasa.gov/W3Browse/all/gcvs.html>

ing model. We changed it to the newly calculated model with CALC3/MSOLV (Jike et al. 2005; Manabe et al. 1991) software package. The new recalculated model contains an estimation of the wet component of atmosphere from GPS data at each VERA station (Honma et al. 2008). We made the images of maser spots associated with R UMa using a task IMAGR. The field of view of each image was $81.92 \text{ mas} \times 81.92 \text{ mas}$ with a pixel size of $0.04 \text{ mas} \times 0.04 \text{ mas}$. With a typical integration time of 5.7 hours, rms noise levels of the phase-referenced images ranged from $0.06 \text{ Jy beam}^{-1}$ to $0.76 \text{ Jy beam}^{-1}$. As a detection criterion of the maser spot on phase-referenced images, we adopted a signal-to-noise ratio (S/N) of 5. For each observation, we fitted an observed brightness distribution with a two-dimensional Gaussian model and adopted its peak as positions of the maser spot. Then, these positions are used to derive a parallax and linear proper motions of the detected maser spots.

Table 1. Coordinates of the sources.

Source	RA (J2000.0)	DEC (J2000.0)
R UMa	$10^{\text{h}} 44^{\text{m}} 38^{\text{s}}.42831$	$+68^{\circ} 46' 32''.3442$
J1056+7011	$10^{\text{h}} 56^{\text{m}} 53^{\text{s}}.61517$	$+70^{\circ} 11' 45''.91561$

2.2 Single-dish observations

In parallel with the VLBI observations, a total power spectrum of H_2O maser has been monitored at the VERA Iriki station with a typical interval of one month in a single-dish monitoring program that started in 2003 September (Shintani et al. 2008). The conversion factor from the antenna temperature to the flux density is about 20 Jy K^{-1} . The $1\text{-}\sigma$ noise level of the single-dish observations is 0.05 K, corresponding to $\sim 1 \text{ Jy}$, in integration time of 10 to 30 min.

2.3 Near-infrared observations

We also carried out near-infrared observations of R UMa from January 2007 to May 2009 using Kagoshima University 1m telescope. The near-infrared camera equipped with the telescope has a 512×512 pixels HAWAII arrays which provides the J -, H -, and K -band images. An image scale of the array is $0''.636 \text{ pixel}^{-1}$, yielding a field of view of $5'.025 \times 5'.025$.

The data reduction and photometry for these data were carried out using the National Optical Astronomy Observatory's Imaging Reduction and Facility (IRAF) software package. Standard procedures of data reduction were adopted. Subtracting the average dark frame, normalizing each of the dark-subtracted images by the flat-field frame, then the sky frame was subtracted from the normalized image. The photometry was carried out with the IRAF/APPHOT package. Since R UMa is bright in near-infrared and it causes a saturation of the detector, we used defocused images for the photometry.

3 Results

3.1 Single-dish results at Iriki station

From the single-dish monitoring at Iriki, we obtained spectral profile and time variation of H_2O maser emissions of R UMa. Figure 1 shows a total power spectra obtained on 2006 Feb 23 (top), Sep 22 (middle) and 2008 Jul 20 (bottom), showing five major velocity components. Noise floors of each spectrum are shifted by 150 and 100 Jy. Figure 2 shows a time variation of the five components at LSR velocity (V_{LSR}) of 38.7 (filled square), 39.7 (open triangle), 40.1 (filled triangle), 41.1 (open circle), and 42.4 (filled circle) km s^{-1} from 2006 to 2008. A velocity component at V_{LSR} of 38.7 km s^{-1} has been dominant among all velocity components during our monitoring period. Same symbols are used in figure 1 and figure 2 to denote each velocity component.

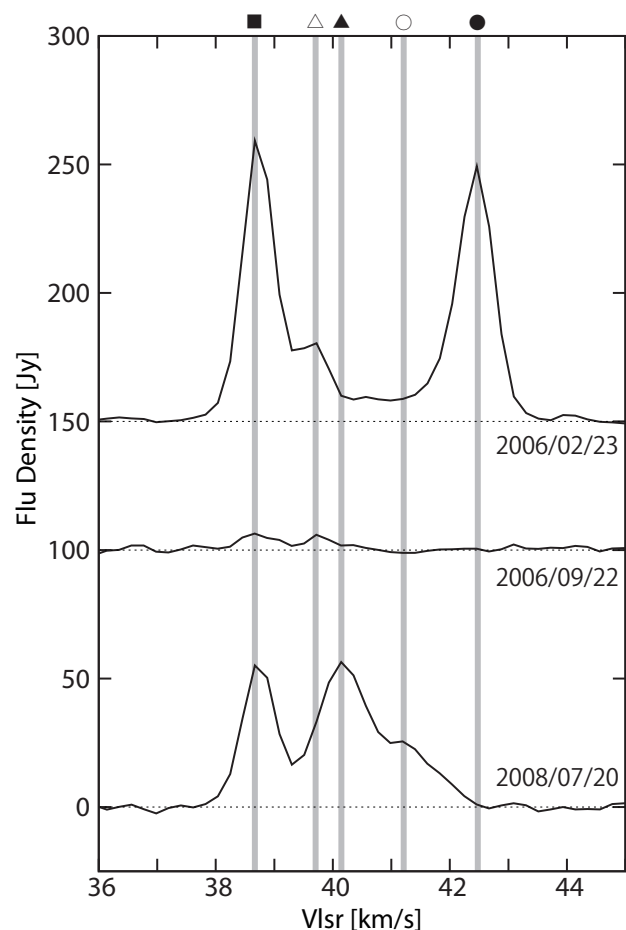


Fig. 1. Total power spectra of H_2O maser in R UMa observed at VERA Iriki station in 2006 Feb 23, Sep 22, and 2008 Jul 20. Vertical grey lines and symbols indicate five major velocity components at V_{LSR} of 38.7 (filled square), 39.7 (open triangle), 40.1 (filled triangle), 41.1 (open circle), and 42.4 (filled circle) km s^{-1} , respectively. Noise floors of each spectrum are presented with dotted horizontal lines.

Table 2. Status of the VLBI observations

Obs. ID	Date			MJD	Days from 2006/1/1	T_{sys} [K]			
	Y	M	D			MIZ	IRK	OGA	ISG
1	2006	Apr	11	53836	101	200–1000	200–1400	200–500	300–500
2		May	14	53869	134	130–190	160–260	200–450	500–8700
3		Aug	13	53960	225	300–13000	300–9800	400–3400	300–700
4		Aug	30	53977	242	200–400	400–13000	300–3000	400–9000
5		Sep	12	53988	255	300–600	400–13000	300–700	400–2000
6		Oct	13	54021	286	150–200	150–200	500–15000	300–800
7		Oct	29	54037	302	150–200	150–200	400–800	400–1200
8		Nov	23	54062	327	100–150	200–1000	300–700	300–1800
9		Dec	21	54090	355	100–150	100–150	400–900	200–2300
10	2007	Jan	20	54120	385	100–150	200–500	200–450	300–12000
11		Feb	23	54154	419	100–150	100–150	150–12000	200–400
12		Apr	04	54194	459	100–150	100–200	150–300	200–500
13		May	09	54229	494	150–250	100–200	300–1800	200–350
14		Sep	11	54354	619	200–1400	200–400	300–450	400–800
15		Oct	14	54387	652	150–200	150–250	...	350–800
16		Nov	13	54417	682	150–200	200–300	150–300	200–1000
17		Dec	14	54448	713	100–200	150–300	150–300	200–800
18	2008	Jan	11	54476	741	200–700	200–750	200–400	300–800
19		Feb	11	54507	772	100–200	200–500	200–300	300–2200
20		Mar	08	54533	798	100–150	100–200	150–200	200–500
21		Apr	02	54558	823	100–200	200–900	150–200	500–4000
22		May	05	54591	856	300–4000	150–400	200–300	400–8000
23		Jun	01	54618	883	200–400	200–600	400–12000	400–5000
24		Jul	06	54653	918	300–600	300–800	300–450	400–2000

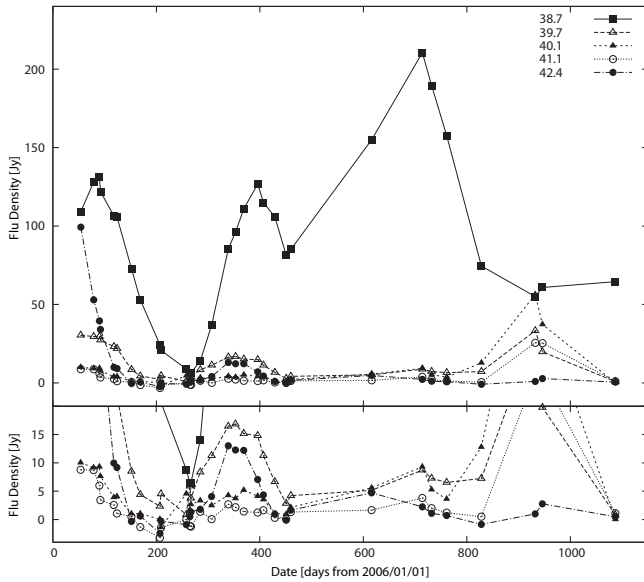


Fig. 2. Time variation of H_2O maser emissions of the five major velocity components from 2006 Jan 1. Same symbols as in figure 1 are used to denote each velocity. Variation of weak components of 0 to 20 Jy is magnified in the lower panel.

3.2 Astrometric error estimation

Position errors of a maser spots consist of several factors in phase-referencing VLBI (Honma et al. 2007; Nakagawa et al. 2008). Before we derive a parallax of the source, we mainly consider two error factors in this section, an atmospheric effect and signal-to-noise ratio of the map. At first, we consider a contribution from wet zenith excess path. From data reduction of our previous study (Nakagawa et al. 2008), we derived a typical zenith excess path length to be 30 mm. Using the same procedure in section 4 of Honma et al. (2007), we estimated the position error of 0.08 mas due to this atmospheric effect. Separation angle (1.78°) of the source pair causes a path-length error of 0.93 mm ($= 30 \text{ mm} \times 1.78^\circ / 57^\circ.3/\text{rad}$), which causes a position error of 0.08 mas ($= 0.93 \text{ mm} / 2.3 \times 10^9 \text{ mm}$ where $2.3 \times 10^9 \text{ mm}$ is the maximum baseline length of the VERA). Next, we consider an error which depends on a signal-to-noise ratio (S/N) of the phase-referenced map. Throughout our series of VLBI observations, major and minor axes of a typical synthesized beam are 1.2 mas \times 0.8 mas with a position angle of 155° . Projection of the synthesized beam onto RA and DEC axes gives $\theta_b^x = 0.73 \text{ mas}$ and $\theta_b^y = 1.09 \text{ mas}$, respectively.

We estimated this error contributions as the beam size divided by S/N values. Since the S/N varies from one observation to the next and from one maser spot to the next, we applied their respective S/N values in the parallax fitting process. On the phase-referenced map with high S/N value, the corresponding error was estimated to be, for example, 0.09 mas in RA axis. Conversely, the error was estimated to be 0.22 mas in DEC axis on the map indicating low S/N value. Although the antenna position errors can be another error source in the astrometry, this contribution is one order of magnitude smaller than the others. These position errors were considered in the parallax fitting which is given in the next section.

3.3 Annual parallax and distance of R UMa

From the phase-referencing analysis, we detected H_2O maser spots in 18 observation among the total of 24 observations. In the data reduction of six observations on 2006 Aug 13, Aug 30, Sep 12, 2007 Sep 11, 2008 Jan 11, and Jul 6, we failed to detect maser spots and we could not use these data sets to estimate the parallax. On 2006 Aug 13 and 30, the maser emission was so faint that we could not detect them. Phase-referencing mapping of the data of 2006 Sep 12 was unable because of lacks of wet atmosphere values which is necessary for data reduction. The data recorded on 2007 Sep 11 and 2008 Jan 11 were invalid because of unknown troubles in data acquisition process, therefore we could not obtain any valid solutions from the data. There is a failure in frequency setting of the observation on 2008 Jul 6, and we failed to make phase-referencing map of this data. Detected maser spots represent V_{LSR} range between 38.17 and 42.81 km s^{-1} , corresponds to 23 discrete velocity channels in our data acquisition setting. In table 3, we summarized detection flags of maser spots for each observation using same observation IDs in table 2. The flags “0” and “1” indicate non-detection and detection at corresponding velocity channel.

Although the maser spots in many velocity channels show stable point-like structures on phase-referenced maps, structures at V_{LSR} of 38.38 , 38.59 , 38.80 , and 39.44 km s^{-1} are complicated and unstable. This brings a difficulty for an identification of the maser spots and we excluded them from parallax estimation. Maser spots at seven more velocity channels were also excluded because the observation number of successful detection (flag “1”) is very limited and it is difficult to justify the parallax fitting. In table 3, V_{LSR} of channels not considered in the parallax fitting were presented with daggers (†).

Even in a single velocity channel, there are sometimes several spatially discrete maser spots that show stable structures. As a result, we identified 15 velocity channels and detected the total of 82 maser spots throughout the series of observations. They provide 164 numerical values (RA and DEC positions of

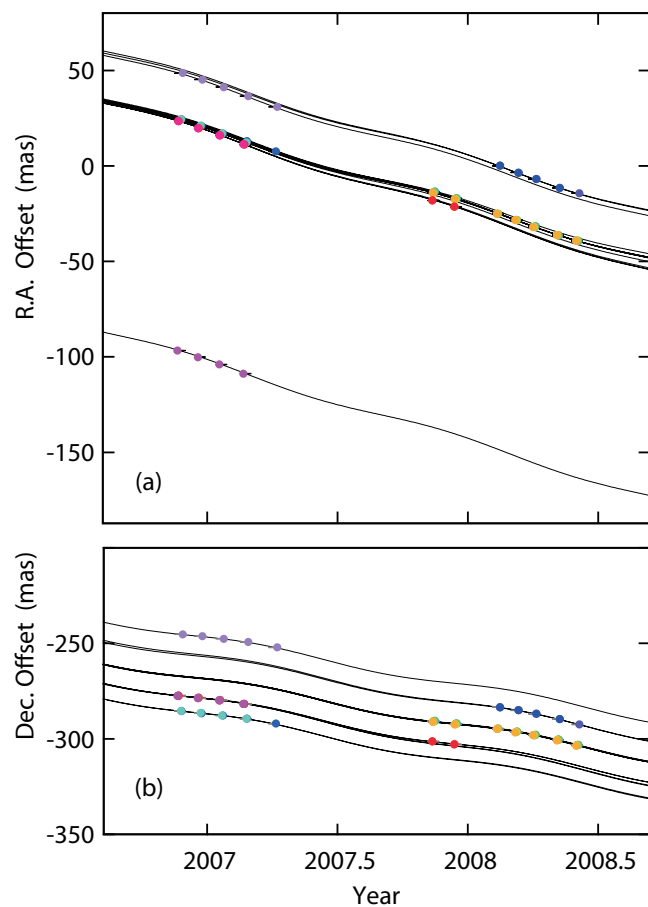


Fig. 3. Position offset of the maser spot in R UMa in RA (a) and DEC (b) along with date. Filled circles and solid lines represent observation data and best fit models, respectively.

each spot). Using these observable values, we solved for 61 free parameters which consist of individual proper motions and initial positions of 15 maser spots along RA and DEC axes, and one common annual parallax. From a least-squares analysis, a parallax was obtained to be 1.97 ± 0.05 mas, corresponds to the distance of 508 ± 13 pc. A reduced-chi square ($= \chi^2/\nu$) of this fitting was calculated to be 1.97, where χ^2 is the squared sum of the residuals of fitting over the square of the uncertainty of each data point, and $\nu (= 164 - 61 = 103)$ is the degree of freedom. The obtained proper motions will be used for an analysis of the internal motions given in section 4.1. Figure 3 (a) and (b) represent motions of the 15 maser spots in RA and DEC axes with respect to defined coordinate of the star. We can see westward and southward systemic motions for all maser spots modulated by parallactic oscillation. In figure 4, we present oscillating terms of the parallactic motion in RA (a) and DEC (b). In both figures, filled circles represent our observation data with error bars, and color denotes velocity, solid lines indicate the best fit models. Symbols in same observation date are plotted with slight shifts along time axis to avoid their overlap.

Table 3. Maser

V_{LSR} [km s ⁻¹]	detection			on			phase						referenced				maps.	
	1	2	6	7	8	9	10	11	12	13	15	16	17	19	20	21		22
42.81 [†]	1	0	0	0	1	1	1	0	0	0	0	0	0	0	0	0	0	0
42.60	1	0	0	0	1	1	1	1	0	0	0	0	0	0	0	0	0	0
42.39	1	1	0	0	1	1	1	1	0	0	1	0	0	0	0	0	0	0
42.18	1	0	0	0	1	1	1	1	0	0	1	1	1	0	0	0	0	0
41.97	0	0	0	0	1	1	1	1	0	0	1	1	1	0	0	0	0	0
41.76 [†]	0	0	0	0	0	0	0	0	0	0	1	1	1	0	0	0	0	0
41.54 [†]	0	0	0	0	0	0	0	0	0	0	1	1	1	0	0	0	0	1
41.33 [†]	0	0	0	0	0	0	0	0	0	0	0	0	0	0	0	0	0	1
41.12 [†]	0	0	0	0	0	0	0	0	0	0	1	0	0	0	0	0	0	1
40.91 [†]	0	0	0	0	0	0	0	0	0	0	1	1	1	0	0	0	0	1
40.70	0	0	0	0	0	0	0	0	0	0	1	1	1	1	1	1	1	1
40.49	0	0	0	0	0	0	0	0	0	0	1	1	1	1	1	1	1	1
40.28	0	0	0	0	0	0	0	0	0	0	1	1	1	1	1	1	1	1
40.07	1	1	0	1	1	1	1	0	0	0	1	1	1	1	1	1	1	1
39.86	1	1	1	1	1	1	1	1	0	0	1	1	1	0	1	1	1	1
39.65	1	1	1	1	1	1	1	1	1	0	1	1	1	0	0	1	1	1
39.44 [†]	1	1	1	1	1	1	1	1	1	0	0	0	1	1	1	0	0	1
39.23	1	1	0	0	0	0	0	0	0	0	0	0	1	1	1	1	1	1
39.02	0	0	0	0	1	1	1	1	1	0	1	1	1	1	1	1	1	1
38.80 [†]	1	1	0	1	1	1	1	1	1	1	1	1	1	1	1	1	1	1
38.59 [†]	1	1	0	1	1	1	1	1	1	1	1	1	1	1	1	1	1	1
38.38 [†]	0	0	0	1	1	1	1	1	1	0	1	1	1	1	1	1	0	0
38.17 [†]	0	0	0	0	0	0	0	1	0	0	1	0	0	0	0	0	0	0

[†] Velocity channels not used in parallax estimation.

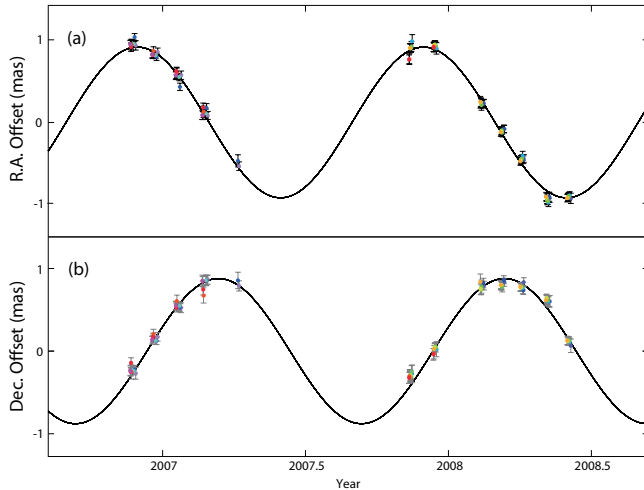


Fig. 4. Parallaxic oscillation along the axes of RA (a) and DEC (b) of the maser spots. Filled circles and solid lines represent observation data and best fit models, respectively.

3.4 Distribution of circumstellar masers

In table 4, we presented all maser spots detected in our phase-referencing analysis. In the V_{LSR} range from 38.17 to 42.81 km s⁻¹, we identified 72 maser spots. Each maser spots moves in accordance with a systemic motion of R UMa. In order to reveal a circumstellar distribution of maser spots on 2006 April 11 (date of the first observation), we calculated their positions by extrapolating initially detected positions using the R UMa's systemic motion in the revised Hipparcos catalog ; $\mu^{\text{HIP}} = (-40.51 \pm 0.79, -22.66 \pm 0.78)$ mas yr⁻¹ (van Leeuwen 2007). Though the Hipparcos measurements have errors, we assumed no error in this calculation. Obtained maser spot positions in RA and DEC (X, Y) are presented in third and fourth columns in table 4. Since flux densities (S) and signal-to-noise ratios (S/N) vary with time, we used these values at their first detection.

Figure 5 shows an obtained distribution of the maser spots in 300 mas square on April 11, 2006. This area corresponds to 152 au square at the source distance estimated by this work, i.e., 508 pc. Filled circles are maser spots, and their colors indicate V_{LSR} between 38 km s⁻¹ (blue) to 43 km s⁻¹ (red). A color in-

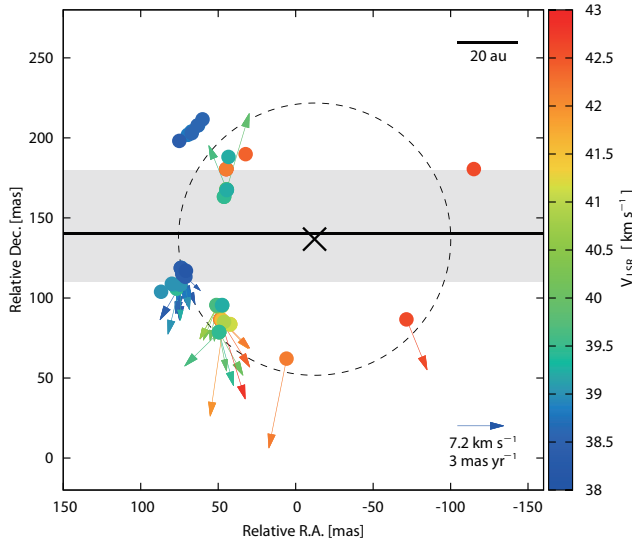


Fig. 5. Distribution and internal motion of maser spots in R UMa. Map angular size of 300 mas square corresponds to 152 au square at the source distance of 508 pc. Filled circles indicate maser spots, and its color indicates V_{LSR} from 38 to 43 km s^{-1} . Horizontal line with peripheral region and cross represent possible positions of the central star. Shell radius of 85 mas is presented with a dotted circle. See section 4.2 for more details.

dex is shown at right of the figure. The majority of maser spots are concentrated in the east of the map, and a few maser spots are detected in the west. Regarding the V_{LSR} property along the DEC axis, there is a large scale velocity gradient from blue- to red-shifted along the east to west direction. Details of arrows in figure 5, which indicate internal motions of the maser spots, will be given in section 4.1.

3.5 Infrared light curve

We carried out near infrared monitoring observations using Kagoshima University 1m telescope. Results of our photometry are presented in table 5. Apparent magnitudes in J -, H -, and K -band at each observation are presented as m_J , m_H , and m_K with their errors. Assuming a sinusoidal function of

$$m_{J/H/K} = \Delta m \sin\left(2\pi \frac{T}{P} + \theta\right) + m_0,$$

we solved pulsation period P , amplitude Δm , and mean magnitude m_0 . We also solved a voluntary phase θ to conduct the numerical fitting. Time is presented as T in the formula.

In figure 6, we show light curves in J - (triangle), H - (square), and K -band (circle) with best fit pulsation models. Three pulsation periods derived from the fitting are consistent within one day, and an averaged period was obtained to be 296.4 days. In K band, mean magnitude and amplitude of pulsation were obtained to be $m_0 = 1.19 \pm 0.02$ mag and $\Delta m = 0.47$ mag, respectively. Other obtained parameters are summarized in table 6.

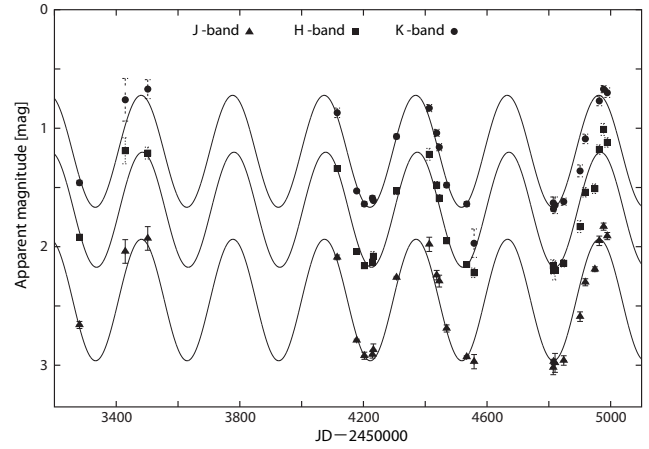


Fig. 6. Infrared light curve of R UMa in J - (triangle), H - (square), and K -bands (circle). Solid lines are best fit pulsation models in each band.

Table 6. Infrared light curve parameters.

Band	P [day]	Δm [mag]	m_0 [mag]
J	296.3	0.51	2.45 ± 0.02
H	296.6	0.49	1.69 ± 0.02
K	296.2	0.47	1.19 ± 0.02
Average	296.4		

P : Pulsation period, Δm : amplitude, m_0 : mean magnitude.

4 Discussion

4.1 Internal motion of circumstellar masers

If we can directly detect a central star with our VLBI method, it is easy to know internal motions of maser spots with respect to the central star. But it is difficult, and we have to introduce some reasonable assumption in order to estimate internal motions of the maser spots. For example, an isotropy of circumstellar kinematics was assumed in our previous study (Nakagawa et al. 2014). In this section, we try to reveal the internal motions of the maser spots with a method using an astrometric measurement from Hipparcos satellite (Perryman et al. 1997).

Proper motions of each maser spot measured in our VLBI observations (μ^{VERA}) involve various kinematics, such as the Galactic rotation, a systemic motion of the star, and their internal motions. A proper motion of R UMa measured by Hipparcos (μ^{HIP}) also include the same kinematics as μ^{VERA} except for internal motions of the maser spots. Therefore, a remainder of two measurements ($\mu^{\text{VERA}} - \mu^{\text{HIP}}$) should give internal motions of the maser spots on the rest frame fixed to the central star. In the revised Hipparcos catalog (van Leeuwen 2007), the proper motion of R UMa is reported to be $\mu^{\text{HIP}} = (-40.51 \pm 0.79, -22.66 \pm 0.78)$ mas yr^{-1} . For maser spots detected more than two continuous epochs, we estimated their

proper motions. Since the parallax of 1.97 mas determined in section 3.3 is the same for all maser spots, we used the fixed parallax and re-fitted all the individual maser spots solving only for internal motion. By subtracting the μ^{HIP} from the proper motions of each maser spot, we obtained internal motions μ_x^{int} and μ_y^{int} for 38 out of all 72 maser spots, and presented them in table 4 in unit of mas yr^{-1} . We also presented errors of the internal motions $\sigma_{\mu_x}^{\text{int}}$ and $\sigma_{\mu_y}^{\text{int}}$ on the table which are quadratic sums of two errors from Hipparcos catalog and our VLBI observation. Since measurement accuracy of proper motions in our VLBI observation is, on average, 0.2 mas yr^{-1} , resultant errors are almost dominated by the error from Hipparcos measurement.

A proper motion of R UMa system can also be estimated from our VLBI observations. We averaged out all the proper motions of maser spots and obtain a motion of $-40.77 \pm 0.39 \text{ mas yr}^{-1}$ and $-24.75 \pm 0.38 \text{ mas yr}^{-1}$ in RA and DEC, respectively. In the RA, two proper motions from Hipparcos and VERA are consistent within their errors. In the DEC, however, there is a difference of $\sim 2 \text{ mas yr}^{-1}$ between two measurements. As shown in figure 5, we found unisotropic distribution of maser spots. We think the systemic motion derived from VERA possibly be biased due to this unisotropy. Therefore, in this section, we used the proper motion in Hipparcos catalog to inspect internal motions of the maser spots.

In figure 5, internal motions of maser spots on sky plane are indicated with arrows. Proper motion of 1 mas yr^{-1} corresponds to a transverse velocity of 2.41 km s^{-1} at the source distance of 508 pc. An arrow at bottom right shows a proper motion of 3 mas yr^{-1} ($= 7.22 \text{ km s}^{-1}$). Average errors of internal motions are 0.90 mas yr^{-1} and 0.88 mas yr^{-1} in RA and DEC, respectively.

Most μ_y^{int} show essentially larger velocities than their errors $\sigma_{\mu_y}^{\text{int}}$, and therefore, we think our analysis gives an reliable picture of the internal motions especially along DEC axis. Maser spots at the southern area of the map show southward motions, and on the contrary, two spots at the northern area show northward motions. With regards to the RA axis, μ_x^{int} values are same as their errors, and this brings a large uncertainty to directions about the internal motions along RA axis. Nevertheless, we can conclude that there is no remarkable systemic motion along RA axis enough to be detected with this method. As a result, our analysis of internal motion revealed an outward motions with respect to the central region of the map. A root sum square of internal motions along two axes ($= \sqrt{(\mu_x^{\text{int}})^2 + (\mu_y^{\text{int}})^2}$) gives a transverse velocities on the skyplane. An average of the transverse velocities was obtained to be 6.61 km s^{-1} . In the next section, we will give a more detailed study to capture a global picture of the maser spots and the central star.

Finally in this subsection, we mention a binarity of the R UMa system. There are some AGB samples known as a bi-

nary stars, i.e., Mira AB system (Karovska et al. 1997), R Aqr (Willson et al. 1981), and so on. The R UMa is one of possible samples of binary system. Sahai et al. (2008) studied fluxes of some AGB stars at near-UV, far-UV, optical, and near-IR bands. They concluded that the far-UV excess likely results either directly from the presence of a hot binary companion or indirectly from a hot accretion disk around the companion. If the R UMa forms a binary system and the binarity affects internal motions of maser spots, astrometric measurements of the maser spots include the binary motion. Then, a remainder $\mu^{\text{VERA}} - \mu^{\text{HIP}}$ still have some contribution from the binary motion. However, as presented above, we could not detect any systematic motion for all maser spots but detected expanding like motions. This can implies that there is no large binary effect that seriously disturb our consideration of internal motion. Therefore, we have not considered the binarity in this section.

4.2 Stellar position and 3D-picture of the maser spots

Based on the distribution and internal motions of the maser spots revealed in previous sections, we will discuss the position of the central star. Now we focus on the motions of the maser spots along DEC axis. In figure 7, we show a relation between μ_y^{int} and Y of 38 maser spots. Since there seems to be a gradient of μ_y^{int} , we fitted this data to a linear function. Then we obtained a relation of $\mu_y^{\text{int}} = 0.062Y - 8.758$, which is presented with a solid line in figure 7. For $V_y = 0$, this relation gives a $Y = 140.45$, and this Y value can be considered as a possible Y position of the central star. In figure 5, this Y value is presented with a solid horizontal line with peripheral region (gray colored) indicating its error. Along the RA axis, it is difficult to find a gradient, we could not conduct the same analysis as the DEC axis.

Independently, we tried to estimate a stellar position using the angular distribution of maser spots. A cross on the map indicates an estimated stellar position of $(X, Y) = (-12.1, 136.8)$ mas which was obtained by simply calculating medians of two ends in RA and DEC axes. Assuming this position, we calculated angular distances θ of the maser spots from the central star. Here, we introduce a simple uniform expanding shell model (Olson 1977; Reid et al. 1977) of

$$\left(\frac{\theta}{\theta_m}\right)^2 + \left(\frac{V_{\text{LSR}} - V_*}{V_{\text{exp}}}\right)^2 = 1,$$

where θ is an angular distance from the central star, θ_m is the shell radius, V_* is the radial velocity of the star, and V_{exp} is an expansion velocity of the shell. Figure 8 shows a θ vs $(V_{\text{LSR}} - V_*)$ diagram of the 38 maser spots. A shape of the model on this figure shows an ellipse. We assumed a V_* of 40.49 km s^{-1} which is obtained as a center of V_{LSR} values of maser spots. Since a distribution of the data on the $\theta - (V_{\text{LSR}} - V_*)$

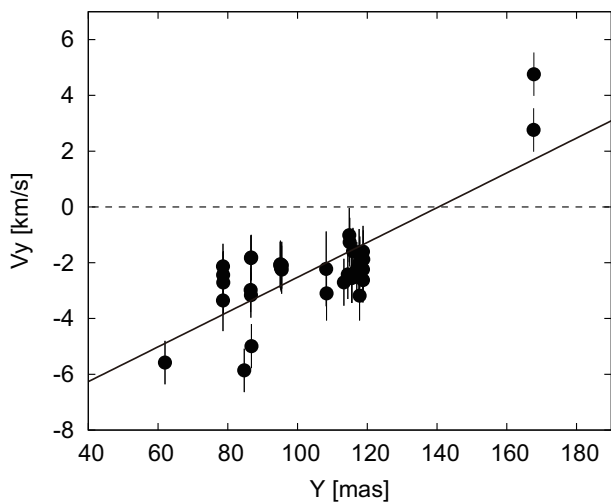


Fig. 7. Velocity gradient of V_y along DEC (Y) axis. An intersection point of $V_y = 0$ and the slope gives $Y = 140.45$ mas.

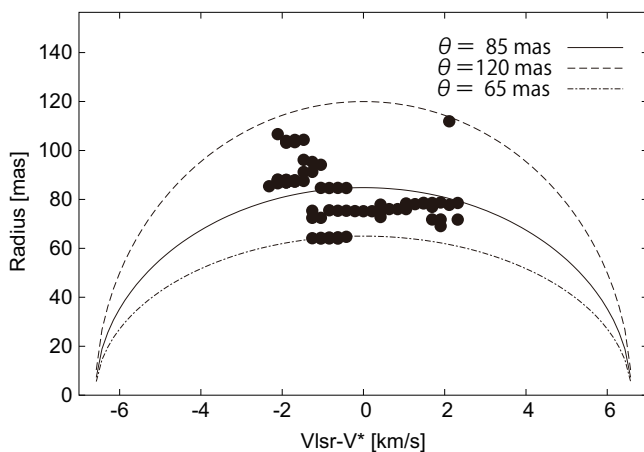


Fig. 8. Relation between an angular radius θ and $V_{\text{LSR}} - V_*$ of the maser spots. A solid ellipse indicates an uniform shell model with a radius of 85 mas obtained from a numerical fitting. Dashed and one-dotted-chain lines indicate models with shell radii of 120 and 65 mas, respectively. Expansion velocities of $V_{\text{exp}} = 6.6 \text{ km s}^{-1}$ are fixed for all models.

plane is too narrow to numerically solve suitable V_{exp} and θ_m , we assumed a V_{exp} to be 6.6 km s^{-1} which is an average of transverse velocities of the maser spots obtained in previous section. Using all maser spots, we solved a θ_m to be 85 ± 2 mas, which is presented with solid line in figure 8. For comparison, we also presented two models whose outer radius of 120 mas (dashed-line) and an inner radius of 65 mas (one-dotted chain line). Latter two models are not obtained from numerical fitting but we assumed fixed radii. In figure 5, the shell model with a radius of $\theta_m = 85$ mas is presented as a dotted circle whose center is assumed to be the cross symbol.

By revealing accurate motion of circumstellar matter, properties of stellar wind will be inspected and it helps us to understand mass-loss process. However, the distributions of circumstellar matter sometimes show symmetry, and sometimes

show asymmetry. A conventional method for determining the circumstellar motion based on the VLBI data, which assumes uniformity or symmetry for circumstellar matters, intrinsically has limitation to derive the real picture. Therefore, it is important to create different method which does not need any assumption about symmetry or uniformity for circumstellar matter. A capability of the new method, which combines VLBI and other independent astrometric data, was presented here. To acquire more accurate picture of internal motions using the same method, accurate systemic motions of stars are required. The Gaia satellite ¹, launched in 2013, is an ongoing astrometric program which expected to measure accurate proper motions for large amount of stars. For very bright stars, like nearby Mira variables, a Japanese satellite Nano-JASMINE ² will also be a powerful and promising telescope to determine their proper motions. In near future, more accurate proper motions of stars measured by new satellites will be tied up with VLBI measurements of maser spots, and circumstellar dynamics of many sources can be studied with the same method in this study. We expect a successful launch of Nano-JASMINE scheduled in near future.

4.3 R UMa in the $M_K - \log P$ Diagram

For AGB stars in the LMC, it is known that there are several distinct sequences on the $m_K - \log P$ diagram (Wood et al. 1999; Ita et al. 2004), where m_K and P indicate their K band apparent magnitude and pulsation period. Sequences C and C' in their classification correspond to groups of variables pulsating in a fundamental tone and a first-overtone, respectively. Since distances of the Galactic sources can not be treated as identical like sources in the LMC, the same relation should be studied in $M_K - \log P$ plane, where M_K is a K band absolute magnitude. In this section, we confirm a location of R UMa on the $M_K - \log P$ plane, and solve a zero-point of the Galactic $M_K - \log P$ relation based on recent astrometric results.

During the last decade, we have conducted astrometric observations for Mira and semiregular variables using VERA (Nakagawa et al. 2008). Determination of $M_K = -8.33 \pm 0.10$ mag of U Lyn by Kamezaki et al. (2015) is the latest published result of Galactic Mira variable based on a parallax from our ongoing program. In this study, using our trigonometric distance of 508 ± 13 pc and the infrared magnitude of $m_K = 1.19 \pm 0.02$ mag, we derived a $M_K = -7.34 \pm 0.06$ mag for R UMa. The error is determined as a root mean square of distance based error and apparent magnitude error. Adding this new source, we summarized the sources in table 7 in an increasing order of pulsation period together with all Galactic LPVs whose distances are determined with astrometric VLBI. There are samples of Mira, semiregular (SRa, SRb in table 7), and red supergiants

¹ Gaia Mission, ESA; <http://sci.esa.int/gaia/>

² Nano - JASMINE, NAOJ ;

<http://www.jasmine-galaxy.org/index-en.html>

(SRC in table 7). Semiregular variables show amplitude smaller than Miras, and among them, stars with better periodicities are referred to as SRa to distinguish from SRb with poorly defined periodicities. Species of the masers used in the parallax measurements are also shown. References of the parallaxes and apparent magnitudes m_K are given in the footnote to table 7. Using the distance and m_K , we derived absolute magnitudes M_K of the sources. In estimation of M_K errors, only the distance errors were considered.

Now, we define a $M_K - \log P$ relation in the form of $M_K = -3.52 \log P + \delta$, where we assume a fixed slope of -3.52 determined by Ita et al. (2004) using LPVs in the LMC. Using Miras and four semiregular variables (RW Lep, S Crt, RX Boo, and W Hya) in table 7, we solved the constant δ . Unweighted and weighted least squares fitting to the data gives δ of 1.09 ± 0.14 and 1.45 ± 0.07 , respectively. In Kamezaki et al. (2012), various periods of a well-studied semiregular source RX Boo are reported, and ratios of the periods are found to be around two. In order to include all Mira and semiregular variables in the fitting, the periods of semiregular variables are multiplied by two and used. Red supergiants are not included in the fitting. Since M_K errors of a few sources are quite small compared to other source, it gives a δ discrepancy of 0.36 between two fittings. In figure 9, we presented all sources in table 7 on $M_K - \log P$ plane with red squares. To distinguish the current result of R UMa from published ones, R UMa is presented with an open square. Two solid lines indicate the results from unweighted (upper) and weighted (lower) fitting, respectively. And, two dashed lines indicate relations derived by Ita et al. (2004) for sequence C' (first-overtone) and C (fundamental tone), respectively. The LPVs in LMC reported by Ita et al. (2004) are presented with small dots in a shaded area of the figure. We can find that R UMa falls on the sequence C, and it is likely that the star pulsates in a fundamental mode. To calibrate absolute magnitudes of the sources in LMC, we assumed a distance modulus of 18.49 (van Leeuwen 2007) for LMC. Within a determination accuracy of δ in our study, we find a consistency of the relations for Mira variables between our Galaxy and the LMC.

In addition to Miras and semiregular variables, now we focus on four sources (3 red supergiants and NML Cyg) in table 7. They are ~ 3 magnitudes brighter than Mira and semiregular variables, and show longer pulsation periods of 822 ($\log P = 2.915$) to 1280 ($\log P = 3.107$) days. If we extrapolate C and C' sequences of Ita et al. (2004) to brighter and longer period region, we find that three sources fall near C' and the other falls near C sequence, that possibly indicating a difference of the pulsation mode. Since the number of the Galactic red supergiants with parallactic distance is small, it is important to increase the sample number for better calibration of their $M_K - \log P$ relation. The VLBI astrometry can be a useful method to provide their accurate distances.

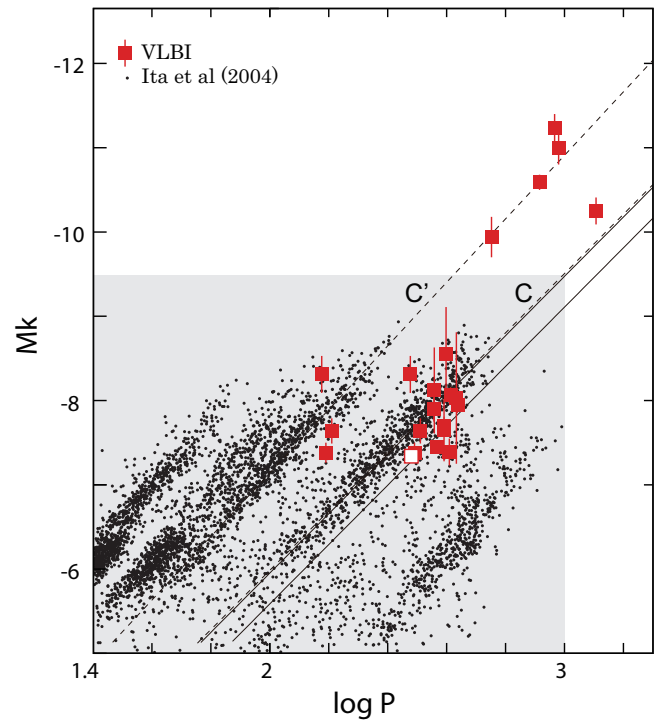


Fig. 9. Absolute magnitudes (M_K) – $\log P$ diagram of the Galactic long period variables. Filled red squares indicate sources in table 7, whose distances are derived from astrometric VLBI. Only the result of R UMa is presented with an open square. Solid lines show fitting results of $M_K - \log P$ relations for Galactic Mira variables in table 7. See section 4.3 for detail of the fitting procedure. In a shaded area, LPVs in the LMC are presented with small dots (Ita et al. 2004). Labels C and C' and corresponding dashed lines indicate sequences in Ita et al. (2004).

4.4 Conclusion

We conducted astrometric VLBI observation of a Mira variable R UMa. Positions of H_2O maser spots at 22 GHz were measured using the VERA array. Obtained parallax of 1.97 ± 0.05 mas gives a distance of 508 ± 13 pc. Circumstellar kinematics of 38 maser spots and angular distribution of all 72 maser spots were revealed from our observations, then we gave a constraint on a stellar position. The $M_K - \log P$ relations for the Galactic LPVs, whose distances were measured from astrometric VLBI, were explored and we obtained the relations of $M_K = -3.52 \log P + (1.09 \pm 0.14)$ and $M_K = -3.52 \log P + (1.45 \pm 0.07)$ from unweighted- and weighted-least squares fittings, respectively. R UMa was found to fall on C sequence that pulsate in a fundamental tone. Positions of red supergiants in the same $M_K - \log P$ plane also found to fall on C' and C sequences. From this we can infer the pulsation mode of the sources, and also this represents an capability of VLBI astrometry for a calibration of $M_K - \log P$ relation applicable to red supergiants.

References

- Asaki, Y., Deguchi, S., Imai, H., et al. 2010, *ApJ*, 721, 267
- Choi, Y. K., Hirota, T., Honma, M., et al. 2008, *PASJ*, 60, 1007
- Cutri, R. M., Skrutskie, M. F., van Dyk, S., et al. 2003, *VizieR Online Data Catalog*, 2246,
- Ducati, J. R. 2002, *VizieR Online Data Catalog*, 2237
- Feast, M. W., Glass, I. S., Whitelock, P. A., & Catchpole, R. M. 1989, *MNRAS*, 241, 375
- Gail, H.-P., & Sedlmayr, E. 2014, *Physics and Chemistry of Circumstellar Dust Shells*, by Hans-Peter Gail, Erwin Sedlmayr, Cambridge, UK: Cambridge University Press, 2014
- Habing, H. J., & Olofsson, H. 2003, *Asymptotic giant branch stars*, by Harm J. Habing and Hans Olofsson. *Astronomy and astrophysics library*, New York, Berlin: Springer, 2003
- Honma, M., et al. 2007, *PASJ*, 59, 889
- Honma, M., Kijima, M., Suda, H., et al. 2008, *PASJ*, 60, 935
- Ita, Y., Tanabé, T., Matsunaga, N., et al. 2004, *MNRAS*, 347, 720
- Jike, T., Fukuzaki, Y., Shibuya, K., Doi, K., Manabe, S., Jauncey, D. L., Nicolson, G. D., & McCulloch, P. M. 2005, *Polar Geosci.*, 18, 26
- Kamezaki, T., Nakagawa, A., Omodaka, T., et al. 2012, *PASJ*, 64, 7
- Kamezaki, T., Kurayama, T., Nakagawa, A., et al. 2014, *PASJ*, 118
- Kamezaki, T., Nakagawa, A., Omodaka, T., et al. 2015, *PASJ*, 208
- Kamohara, R., Bujarrabal, V., Honma, M., et al. 2010, *A&A*, 510, A69
- Karovska, M., Hack, W., Raymond, J., & Guinan, E. 1997, *ApJL*, 482, L175
- Kawaguchi, N., Sasao, T., & Manabe, S. 2000, *Proc. SPIE*, 4015, 544
- Knapp, G. R., Crosas, M., Young, K., & Ivezić, Ž. 2000, *ApJ*, 534, 324
- Kobayashi, H., et al. 2003, *ASP Conference Series*, 306, 48P
- Kurayama, T., Sasao, T., & Kobayashi, H. 2005, *ApJL*, 627, L49
- Kusuno, K., Asaki, Y., Imai, H., & Oyama, T. 2013, *ApJ*, 774, 107
- Manabe, S., Yokoyama, K., & Sakai, S. 1991, *IERS Techn. Note*, 8, 61
- Min, C., Matsumoto, N., Kim, M. K., et al. 2014, *PASJ*, 66, 38
- Nakagawa, A., Tsushima, M., Ando, K., et al. 2008, *PASJ*, 60, 1013
- Nakagawa, A., Omodaka, T., Handa, T., et al. 2014, *PASJ*, 66, 101
- Nyu, D., Nakagawa, A., Matsui, M., et al. 2011, *PASJ*, 63, 63
- Olson, F. M. 1977, Ph.D. Thesis, Univ. Leiden
- Perryman, M. A. C., et al. 1997, *A&A*, 323, L49
- Reid, M. J., Muhleman, D. O., Moran, J. M., Johnston, K. J., & Schwartz, P. R. 1977, *ApJ*, 214, 60
- Sahai, R., Findeisen, K., Gil de Paz, A., & Sánchez Contreras, C. 2008, *ApJ*, 689, 1274
- Shibata, K. M., Kameno, S., Inoue, M., & Kobayashi, H. 1998, *IAU Colloq. 164: Radio Emission from Galactic and Extragalactic Compact Sources*, 144, 413
- Shintani, M., Imai, H., Ando, K., et al. 2008, *PASJ*, 60, 1077
- van Leeuwen, F. 2007, *Hipparcos, the New Reduction of the Raw Data*. By Floor van Leeuwen, Institute of Astronomy, Cambridge University, Cambridge, UK Series: *Astrophysics and Space Science Library*
- Vlemmings, W. H. T., van Langevelde, H. J., Diamond, P. J., Habing, H. J., & Schilizzi, R. T. 2003, *A&A*, 407, 213
- Vlemmings, W. H. T., & van Langevelde, H. J. 2007, *A&A*, 472, 547
- Whitelock, P., Menzies, J., Feast, M., et al. 1994, *MNRAS*, 267, 711
- Whitelock, P., & Feast, M. 2000, *MNRAS*, 319, 759
- Willson, L. A., Garnavich, P., & Mattei, J. A. 1981, *Information Bulletin on Variable Stars*, 1961, 1
- Wood, P. R., Alcock, C., Allsman, R. A., et al. 1999, *Asymptotic Giant Branch Stars*, 191, 151
- Zhang, B., Reid, M. J., Menten, K. M., Zheng, X. W., & Brunthaler, A. 2012, *A&A*, 544, AA42

Table 4. Parameters of the detected masers.

ID	V_{LSR}	X	Y	S	S/N	μ_x^{int}	$\sigma_{\mu x}^{\text{int}}$	μ_y^{int}	$\sigma_{\mu y}^{\text{int}}$
i	[km s $^{-1}$]	[mas]	[mas]	[Jybeam $^{-1}$]		[mas yr $^{-1}$]		[mas yr $^{-1}$]	
1	42.81	44.87	180.43	3.03	15.5
2	42.81	48.47	86.77	0.79	7.3	-1.59	1.30	-4.99	0.79
3	42.6	-115.15	180.49	5.41	15.9
4	42.6	-71.55	86.61	1.67	13.2	-1.34	0.86	-3.16	0.81
5	42.39	44.86	180.50	4.36	15.3
6	42.39	32.27	189.81	0.43	3.9
7	42.39	48.48	86.55	2.1	16.4	-1.89	0.88	-2.98	0.79
8	42.18	44.82	180.57	1.99	11.8
9	42.18	48.42	86.71	1.25	11.7	-1.88	0.80	-1.81	0.81
10	42.18	5.86	61.99	1.36	10.4	1.15	0.79	-5.58	0.78
11	41.97	48.40	86.62	0.73	7.3	-1.79	0.79	-1.83	0.81
12	41.97	46.42	84.72	1.5	7.9	0.87	0.79	-5.86	0.78
13	41.76	46.42	85.11	0.95	10.6
14	41.54	47.67	86.17	0.7	4.9
15	41.54	42.32	83.72	1.37	10
16	41.33	42.28	83.62	1.93	15.7
17	41.12	42.23	83.60	1.61	12.2
18	40.91	50.30	94.94	1.83	7.4
19	40.91	46.11	85.07	0.56	7.1
20	40.91	47.50	94.99	0.95	7.3
21	40.7	50.41	95.04	3.93	11.9	1.13	0.81	-2.08	0.83
22	40.49	50.42	95.09	4.88	12.3	1.14	0.81	-2.05	0.84
23	40.28	50.54	95.20	4.66	12.6	0.89	0.83	-2.14	0.83
24	40.07	44.62	167.91	1.41	9.5
25	40.07	49.47	78.73	1.54	13.5	-1.56	0.89	-2.71	1.13
26	40.07	50.74	95.28	3.37	12.5	0.45	0.84	-2.20	0.83
27	39.86	44.55	167.77	3.5	14.7	-1.46	0.79	4.76	0.78
28	39.86	46.24	163.17	1.5	7
29	39.86	49.44	78.65	4.38	22.5	-0.49	0.95	-2.44	0.82
30	39.86	50.89	95.45	1.86	8.6	0.16	0.83	-2.25	0.86
31	39.65	44.41	167.71	4.27	15.3	1.17	0.79	2.76	0.78
32	39.65	46.20	163.31	1.47	7.1
33	39.65	49.39	78.63	4.76	24.1	2.23	1.22	-2.13	0.81
34	39.65	51.15	95.49	0.91	5.5	-0.23	0.90	-2.09	0.84
35	39.44	44.35	167.57	2.34	11.1
36	39.44	46.21	163.19	0.83	4.6
37	39.44	49.40	78.61	1.79	13.9	-0.94	1.43	-3.35	1.10
38	39.44	76.83	105.81	0.96	8.8
39	39.44	47.48	95.53	3.19	23.2
40	39.23	44.32	167.28	1	7.6
41	39.23	43.21	188.00	0.46	4.4
42	39.23	78.81	108.18	2.06	14.4
43	39.23	74.58	108.22	1.93	13.7	-0.02	1.14	-2.22	1.34
44	39.23	47.45	95.47	0.99	8
45	39.02	73.57	118.77	1.01	9.6	-0.51	0.80	-2.62	0.81
46	39.02	86.94	103.90	1.91	5.2
47	39.02	79.91	108.88	2.64	13.8
48	39.02	74.54	108.32	3.03	16.7	0.79	0.95	-3.10	0.97

Table 4. (Continued)

ID	V_{LSR}	X	Y	S	S/N	μ_x^{int}	$\sigma_{\mu_x}^{\text{int}}$	μ_y^{int}	$\sigma_{\mu_y}^{\text{int}}$
i	[km s ⁻¹]	[mas]	[mas]	[Jybeam ⁻¹]		[mas yr ⁻¹]		[mas yr ⁻¹]	
49	38.8	69.53	201.79	1.29	7.1
50	38.8	63.10	207.75	0.99	8
51	38.8	67.36	203.96	0.93	7.6
52	38.8	73.86	118.84	2.18	12.7	-0.46	0.95	-1.88	1.04
53	38.8	73.07	117.85	4.52	6.3	0.37	0.82	-1.98	0.92
54	38.8	73.16	117.80	1.63	9.5	-0.18	0.85	-2.03	0.84
55	38.8	72.99	115.91	1.03	5.3	-0.52	0.80	-1.59	0.84
56	38.59	60.03	211.63	1.27	6.3
57	38.59	63.39	207.86	0.85	5.2
58	38.59	67.08	202.93	1.13	8.3
59	38.59	73.98	118.80	1.89	9.4	-0.60	0.84	-1.60	0.92
60	38.59	72.50	116.98	7.39	12.9	0.28	0.82	-2.23	0.97
61	38.59	73.13	117.65	2.16	10.7	-0.09	0.83	-1.62	0.83
62	38.59	72.23	115.53	4.72	6.2	0.48	0.83	-2.52	0.92
63	38.59	73.12	114.96	0.95	4.7	-0.16	1.05	-1.26	0.87
64	38.59	72.01	114.43	4.13	10.1	0.56	0.97	-2.42	0.88
65	38.38	75.19	198.07	0.62	5.8
66	38.38	74.19	118.79	0.73	6.1	-0.93	0.92	-2.24	0.88
67	38.38	73.27	117.79	1.95	4.2	0.18	0.81	-3.18	0.89
68	38.38	73.20	117.60	0.92	7.6	-0.33	0.91	-2.27	0.81
69	38.38	72.21	115.58	3.11	6.7	0.41	0.81	-2.55	0.89
70	38.38	72.95	114.83	0.57	4.8	-1.14	1.04	-1.01	0.97
71	38.38	71.24	113.29	2.51	5.4	1.64	0.90	-2.70	0.84
72	38.17	70.90	116.85	0.61	9.3

Column (1)—Component ID. Column (2)—LSR velocity in km s⁻¹. Column (3)—positions in RA relative to the original phase center. Column (4)—positions in DEC relative to the original phase center. Column (5)—brightness of the spot at the first detection in Jy beam⁻¹. Column (6)—signal-to-noise ratio (S/N). Column (7)—best fit linear internal motion in RA in mas yr⁻¹. Column (8)—standard errors of the motion in RA. Column (9)—best fit linear internal motion in DEC in mas yr⁻¹. Column (10)—standard errors of the motion in DEC.

Table 5. *J*-, *H*-, *K*-band magnitudes.

MJD	m_J [mag]	m_H [mag]	m_K [mag]
53132	2.13±0.03	1.35±0.06	0.94±0.07
53281	2.66±0.03	1.92±0.02	1.46±0.02
53429	2.04±0.10	1.19±0.11	0.76±0.18
53502	1.93±0.10	1.21±0.05	0.67±0.08
54115	2.09±0.02	1.34±0.02	0.87±0.04
54178	2.79±0.01	2.04±0.02	1.53±0.01
54203	2.92±0.03	2.16±0.02	1.64±0.02
54229	2.91±0.03	2.13±0.01	1.59±0.02
54232	2.87±0.05	2.08±0.04	1.61±0.01
54307	2.26±0.01	1.53±0.03	1.07±0.02
54413	1.98±0.06	1.22±0.05	0.83±0.03
54437	2.24±0.04	1.48±0.03	1.04±0.03
54445	2.29±0.05	1.59±0.03	1.16±0.03
54469	2.69±0.03	1.95±0.02	1.48±0.02
54534	2.93±0.01	2.15±0.01	1.64±0.02
54558	2.97±0.06	2.22±0.04	1.97±0.12
54814	3.02±0.06	2.16±0.05	1.63±0.05
54815	2.97±0.02	2.20±0.03	1.68±0.02
54820	2.98±0.08	2.20±0.08	1.65±0.07
54848	2.96±0.04	2.14±0.03	1.62±0.03
54901	2.59±0.04	1.83±0.05	1.36±0.05
54918	2.30±0.03	1.54±0.04	1.09±0.04
54949	2.19±0.02	1.51±0.04	—
54963	1.95±0.04	1.18±0.04	0.77±0.04
54977	1.83±0.03	1.01±0.05	0.67±0.03
54989	1.91±0.03	1.12±0.04	0.70±0.04

Table 7. Results from VLBI astrometry

Source	Type	Parallax [mas]	P [day]	$\log P$	m_K [mag]	M_K [mag]	Maser	Reference [†] (Parallax, m_K)
RW Lep	SRa	1.62±0.16	150	2.176	0.639	-8.31 ± 0.22	H ₂ O	kam14, a
S Crt	SRb	2.33±0.13	155	2.190	0.786	-7.38 ± 0.12	H ₂ O	nak08, a
RX Boo	SRb	7.31±0.5	162	2.210	-1.96	-7.64 ± 0.15	H ₂ O	kam12, b
R UMa	Mira	1.97±0.05	302	2.480	1.19	-7.34 ± 0.06	H ₂ O	...
W Hya	SRa	10.18±2.36	361	2.558	-3.16	-8.12 ± 0.51	OH	vle03, c
S CrB	Mira	2.39±0.17	360	2.556	0.21	-7.90 ± 0.15	OH	vle07, c
T Lep	Mira	3.06±0.04	368	2.566	0.12	-7.45 ± 0.03	H ₂ O	nak14, c
R Aqr	Mira	4.7±0.8	390	2.591	-1.01	-7.65 ± 0.37	SiO	kam10, c
R Aqr	Mira	4.59±0.24	390	2.591	-1.01	-7.70 ± 0.11	SiO	min14, c
RR Aql	Mira	1.58±0.40	396	2.598	0.46	-8.55 ± 0.56	OH	vle07, c
U Her	Mira	3.76±0.27	406	2.609	-0.27	-7.39 ± 0.16	OH	vle07, c
SY Scl	Mira	0.75±0.03	411	2.614	2.55	-8.07 ± 0.09	H ₂ O	nyu11, b
R Cas	Mira	5.67±1.95	430	2.633	-1.80	-8.03 ± 0.78	OH	vle03, c
U Lyn	Mira	1.27±0.06	434	2.637	1.533	-7.95 ± 0.10	H ₂ O	kam15, a
UX Cyg	Mira	0.54±0.06	565	2.752	1.40	-9.94 ± 0.24	H ₂ O	kur05, a
S Per	SRc	0.413±0.017	822	2.915	1.33	-10.59 ± 0.09	H ₂ O	asa10, b
PZ Cas	SRc	0.356±0.026	925	2.966	1.00	-11.24 ± 0.16	H ₂ O	kus13, b
VY CMa	SRc	0.88±0.08	956	2.980	-0.72	-11.00 ± 0.20	H ₂ O	cho08, b
NML Cyg	—	0.62±0.047	1280	3.107	0.791	-10.25 ± 0.16	H ₂ O	zha12, a

[†] References of the parallax are as follows : (kam14) Kamezaki et al. 2014, (nak08) Nakagawa et al. 2008, (kam12) Kamezaki et al. 2012, (vle03) Vlemmings et al. 2003, (vle07) Vlemmings & van Langevelde 2007, (nak14) Nakagawa et al. 2014, (kam10) Kamohara et al. 2010, (min14) Min et al. 2014, (nyu11) Nyu et al. 2011, (kam15) Kamezaki et al. 2015, (kur05) Kurayama et al. 2005, (asa10) Asaki et al. 2010, (kus13) Kusuno et al. 2013, (cho08) Choi et al. 2008, and (zha12) Zhang et al. 2012. References of the apparent magnitudes (m_K) are as follows : (a) The IRSA 2MASS All-Sky Point Source Catalog (Cutri et al. 2003), (b) Catalogue of Stellar Photometry in Johnson's 11-color system (Ducati 2002), (c) Photometry by Whitelock & Feast (2000).